In-situ alloyed, oxide-dispersion-strengthened CoCrFeMnNi high entropy alloy fabricated via laser powder bed fusion

Chen, Peng; Yang, Chao; Li, Sheng; Attallah, Moataz M.; Yan, Ming

DOI:
10.1016/j.matdes.2020.108966

Document Version
Publisher's PDF, also known as Version of record

Citation for published version (Harvard):
Chen, P, Yang, C, Li, S, Attallah, MM & Yan, M 2020, 'In-situ alloyed, oxide-dispersion-strengthened CoCrFeMnNi high entropy alloy fabricated via laser powder bed fusion', *Materials and Design*, vol. 194, 108966. https://doi.org/10.1016/j.matdes.2020.108966

Materials and Design 194 (2020) 108966

Contents lists available at ScienceDirect

Materials and Design

journal homepage: www.elsevier.com/locate/matdes

In-situ alloyed, oxide-dispersion-strengthened CoCrFeMnNi high entropy alloy fabricated via laser powder bed fusion

Peng Chen [a,b], Chao Yang [c], Sheng Li [b], Moataz M. Attallah [b,*], Ming Yan [a,*]

[a] Department of Materials Science and Engineering, Southern University of Science and Technology, Shenzhen 518055, China
[b] School of Metallurgy and Materials, University of Birmingham, Birmingham B15 2TT, UK
[c] School of Mechanical and Automotive Engineering, South China University of Technology, Guangzhou 510641, China

HIGHLIGHTS

- Oxide-dispersion-strengthened CoCrFeMnNi high entropy alloy has been in-situ alloyed via laser powder bed fusion.
- The forming mechanism of the oxide particles has been revealed.
- The tensile strength is mainly improved by Orowan strengthening.

GRAPHICAL ABSTRACT

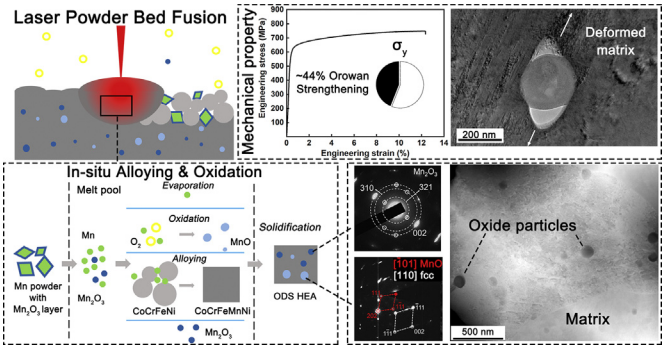

ARTICLE INFO

Article history:
Received 29 April 2020
Received in revised form 17 June 2020
Accepted 8 July 2020
Available online 11 July 2020

Keywords:
High entropy alloys
Powder bed fusion
Additive manufacturing
Deformation behaviour
Orowan strengthening

ABSTRACT

By using a blend of pre-alloyed CoCrFeNi powder and elemental Mn powder, quasi-equiatomic CoCrFeMnNi high entropy alloy (HEA) has been in-situ alloyed via laser powder bed fusion (LPBF). Besides being homogeneously dissolved into the HEA matrix, Mn also forms oxide particles with oxygen originating from both powder feedstock and printing atmosphere, resulting in an in-situ alloyed, oxide-dispersion-strengthened (ODS) HEA. The tensile strength of the ODS HEA is significantly improved to a yield strength of 620 MPa and a tensile strength of 730 MPa. The tensile ductility of the ODS HEA is lower than the ones prepared by using fully pre-alloyed powders, but an outstanding compression ductility maintains for the ODS HEA. The deforming behaviour of the alloy has been revealed, and the contribution of Orowan strengthening has been quantified along with other mechanisms. The study provides an approach to developing advanced HEAs with high strength and moderate ductility by LPBF.

1. Introduction

The discovery of high entropy alloys (HEAs) is one of the most significant developments in the field of metallic materials. The concept of HEA allows researchers to choose multi-principal elements in one HEA system, each concentration between 5 and 35 at. %, which composition locates at the normally unexplored central area of a phase diagram [1–3]. At the initial stage of the alloy development, HEAs are requested to form single-phase solid solutions with five or more principal elements at an equiatomic ratio [4]. The definition of HEAs has been evolved with time. For instances, dual-phase solid solution HEAs like $Al_xCoCrFeNi$ are accepted, whose microstructure gradually transforms from ductile face-centric cubic (fcc) phase to brittle body-centric cubic (bcc) phase as the content of Al increases; precipitation-strengthened

* Corresponding authors.
E-mail addresses: M.M.Attallah@bham.ac.uk (M.M. Attallah), yanm@sustech.edu.cn (M. Yan).

https://doi.org/10.1016/j.matdes.2020.108966

HEAs such as fcc-CoCrFeNi reinforced by $L1_2$-Ni_3(Ti, Al) also emerge [5–7]. The great compositional flexibility endows HEAs with the possibility to cover most property maps of knowing alloy systems and even extend to those previously unattainable areas.

HEAs have shown application potential due to their outstanding properties. Conventionally, HEAs are mostly fabricated by arc melting or coating methods to avoid segregation during solidification [3]. But the products fabricated via those techniques can hardly accomplish the requirements of various applications [8]. Manufacturing of HEA parts with chemistry homogeneity, geometry flexibility and excellent mechanical properties is still in the beginning stage.

Laser powder bed fusion (LPBF), also known as selective laser melting (SLM), is a laser-based additive manufacturing (AM) technique that has been widely employed to fabricate metallic parts with complex geometry for many important industries [9,10]. As for HEAs, single-phase fcc HEAs such as CoCrFeNi, CoCrFeMnNi and $Al_{0.5}$FeCoCrNi possess good LPBF printability, when using pre-alloyed powder [11–13]. Heterogeneous pre-alloyed HEA powders have also been developed for LPBF, e.g. CoCrFeNiTi-based HEA, AlCrCuFeNi$_x$ and C-containing CoCrFeNi HEAs [14–18]. Shortcomings of the pre-alloyed powder approach include that the compositional flexibility is restricted, and the production circle can be quite time consuming. Direct laser fabrication (DLF) is another laser-based AM technique, which can deliver different elemental powders simultaneously and melt them in a large molten pool to achieve in-situ alloying. Al_xCoCrFeNi HEA has been in-situ alloyed by DLF, and all compositional elements can be dissolved and homogenised [19]. By this way, the composition of HEAs can be more flexible than using pre-alloyed powder, yet the forming accuracy of DLF is much lower than that of LPBF, which means that a considerable secondary processing is inevitable to produce a qualified part via the DLF in-situ alloying.

To produce HEA parts with both complex geometry and compositional flexibility by AM, a potential solution is the in-situ alloying by LPBF using blended powder rather than pre-alloyed powder. In previous studies, LPBF in-situ alloying has shown its feasibility on introducing a minor amount of elemental powder into conventional alloy systems, e.g. 2 at. % of elemental Al powder has been in-situ alloyed with pre-alloyed In718 powder to precipitate more sigma phase and enhance the mechanical properties; Ti2AlNb has also been in-situ alloyed from a blend of elemental powders [20,21]. However, the small molten pool in the LPBF process encounters with problems like segregation of the introduced element and high cracking tendency due to the generation of secondary phase(s), when the amount of elemental powder increases to a higher level [22]. In this regard, the feasibility of in-situ fabricating HEAs using blended elemental powders via LPBF needs to be further testified.

Based on this consideration, a CoCrFeMnNi HEA has been in-situ alloyed from a blend of pre-alloyed CoCrFeNi powder and elemental Mn powder in our previous research as a pilot study [23]. It shows that the HEA matrix can maintain an fcc structure as the content of dissolved Mn is up to 20 at. %, which is a considerably compositional feasibility achieved via the PBLF in-situ alloying. Aside from good densification and homogeneity, the in-situ alloyed HEA has also shown improved microhardness and oxygen content. More interestingly, a much-enhanced strength has been discovered in the in-situ alloyed HEA, which detailed information needs to be clarified. In this study, the structure-property correlation of the in-situ alloyed HEA is thoroughly analysed. Mn oxide particles are found dispersed extensively in the HEA matrix, resulting in an oxide-dispersion-strengthened (ODS) HEA. Meantime, although ODS HEAs have been produced using spark plasma sintering (SPS) via adding yttria or alumina particles to HEA powder [24,25], in-situ formed ODS HEA is rarely reported for AM techniques [26,27]. Hence, this study investigates the oxides formation mechanism of the in-situ alloyed HEA, which is essential to offering a time- and cost-efficient LPBF route to fabricate advanced ODS parts with excellent mechanical properties particularly in terms of strength.

2. Material and methods

2.1. Powder and LPBF process

A powder blend of pre-alloyed CoCrFeNi powder (TLS Technik GmbH) and elemental Mn powder (Sigma-Aldrich) was used as raw material to fabricate the in-situ alloyed CoCrFeMnNi HEA. The two powders were weighed to ensure quasi-equiatomic composition (Table 1), and then mixed by a horizontal mixing machine for 1 h to pre-homogenise before the LPBF process (Fig. 1(a)). The original atomic percentage of Mn was higher than the nominal 20 at. %, since a selective evaporation of Mn was expected during printing, and the extra amount of Mn may help to compensate for the elemental loss. A Concept Laser M2 was employed to fabricate bulk HEA parts from the blended powder. All samples were fabricated on 316 L stainless steel substrates with argon protection. A schematic of the scanning strategy used in this study is shown in Fig. 1(b). Each layer was separated into chessboard pattern composed of 5×5 mm^2 blocks, with internal scanning routes normal to those in neighbouring blocks. Every block rotated 90° and shifted 1 mm along both x and y-axis in the following layer. The scanning patterns are revealed in Fig. 1(c). The y-axis was marked as the gauge length of tensile specimens as well. The layer thickness (t) was 30 μm for the blended powder. An optimised laser parameter set, including laser power (P) of 280 W, scanning speed (v) of 800 mm/s, and hatch spacing (h) of 60 μm, was applied in the LPBF process, achieving a high relative density [23]. The volumetric energy density (VED) applied in the LPBF process was calculated by $VED = P/(vht)$ [23].

2.2. Microstructural characterisation

Phase formation of the blended powder and LPBFed samples was characterised by X-ray diffraction (XRD) on a Rigaku Smartlab with Cu radiation. To reveal the microstructure of the in-situ alloyed HEA, samples were grounded and then finished by a Buehler VibroMeting 2 Vibratory Polisher. A Zeiss Merlin field emission scanning electron microscope (SEM) equipped with electron back-scattered diffraction (EBSD) and a back-scattered electron (BSE) detectors was employed to reveal the microstructure. Electron channelling contrast imaging (ECCI) was also performed through the BSE detector operated at 30 kV, and the sample holder tilted between 2 and 5°. Samples for transmission electron microscopy (TEM) were prepared via focused ion beam (FIB) using an FEI Helios Nanolab 600i, and then analysed by an FEI Talos F200X equipped with energy dispersive spectrometer (EDS). The surface of the elemental Mn powder was characterised by X-ray photoelectron spectroscopy (XPS) via a PHI 5000 Versaprobe III. An LECO ON736 elemental analyser was employed to measure the oxygen content.

2.3. Mechanical testing

Tensile parts were fabricated according to the model illustrated in Fig. 2. (a), and then separated into tensile specimens with gauge dimension of $25 \times 4.3 \times 2$ mm^3 by electrical discharge machine (EDM). Tensile tests were carried out on an Instron 3382 universal testing machine

Table 1
Chemistry of the blended powder and as-built sample in this study.

		Co	Cr	Fe	Ni	Mn
Blended powder	wt%	79 (pre-alloyed)				21 (elemental)
	at. %	19.93	21.64	18.59	18.31	21.53
As-built HEA (at. %)		21.59	21.88	20.14	19.72	16.67

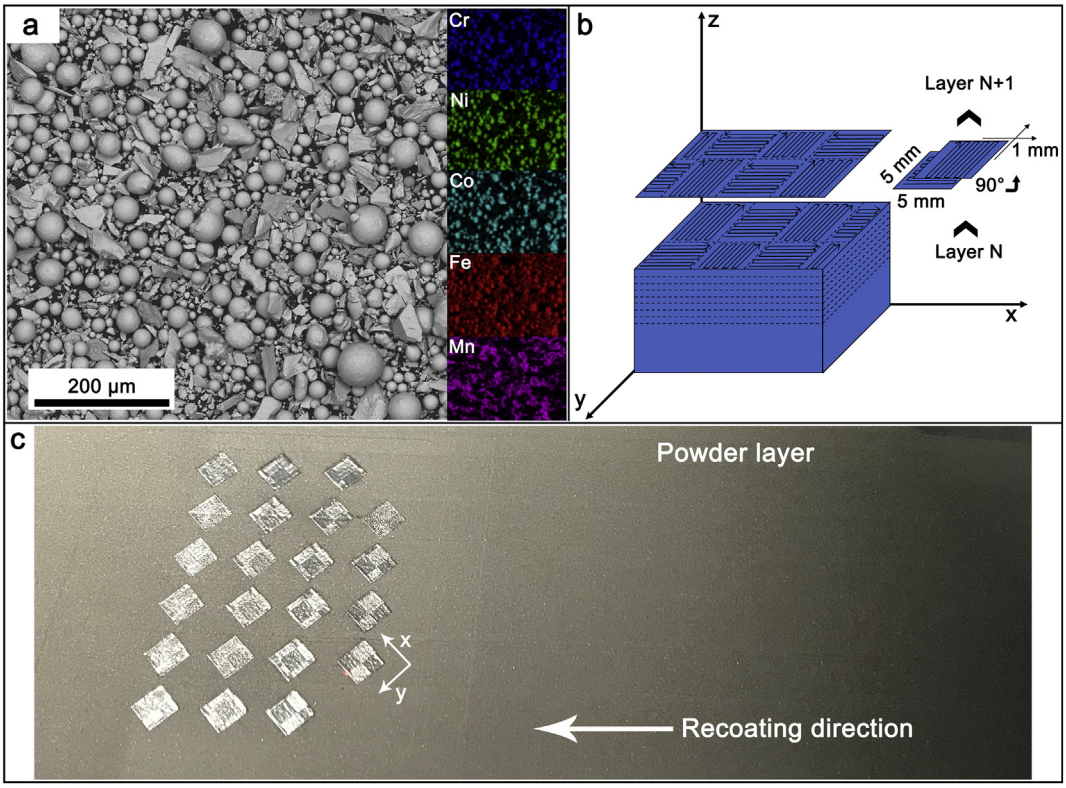

Fig. 1. (a) An SEM image of the blended powder including spherical pre-alloyed powder and irregular-shaped elemental Mn powder, with EDS mapping results of elemental distribution which is similar to powder layer before scanning. (b) A Schematic of the chessboard scanning strategy and (c) a layer scanned by laser in the LPBF process.

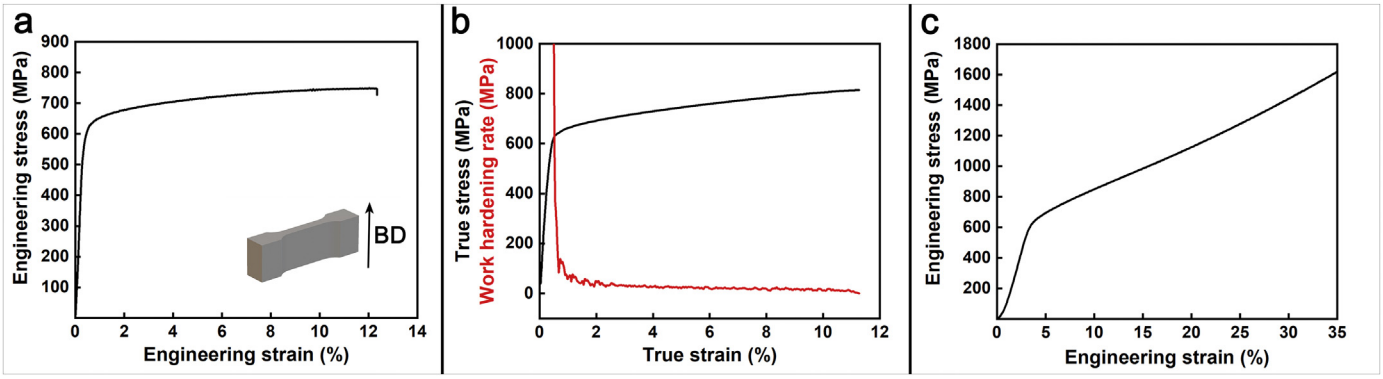

Fig. 2. (a) The tensile curve of the in-situ alloyed HEA, with an embedded demonstration of the tensile model used for the LPBF process. (b) The true stress-strain curve specimen and work hardening rate curve of the tensile specimen. (c) A partial compression curve of the in-situ alloyed HEA.

with an extensometer and controlled at a strain rate of 10^{-3}/s. For compression tests, cylinder specimens with a diameter of 6 mm and a height of 9 mm were produced by EDM from bulk samples. Compression tests were operated at a strain rate of 10^{-3}/s without extensometer.

3. Results

3.1. Mechanical properties of the in-situ alloyed HEA

A representative tensile curve of the in-situ alloyed HEA is plotted in Fig. 1(a). Details of the tensile properties are listed in Table 2, which is compared with results from using pre-alloyed powder to print the CoCrFeMnNi HEA. In comparison, the strength of the in-situ alloyed HEA is significantly improved, but the fracture elongation (ε_f) drops to ~12%, which seems to be a strength-ductility trade-off. The work hardening rate and true stress-strain curves are illustrated in Fig. 2(b). It is recognised that the work hardening rate drops dramatically after the yield point. In contrast, the work hardening effect is considerable in CoCrFeMnNi HEAs that are fabricated using DLD, casting or forging [28–30]. Both the strain-hardening ability and ductility of the

Table 2
Comparison of tensile properties between CoCrFeMnNi HEAs fabricated using blended powder and pre-alloyed powder.

CoCrFeMnNi	VED (J/mm^3)	$\sigma_{0.2}$ (MPa)	σ_{uts} (MPa)	ε_f (%)	d (μm)
In-situ alloyed	194	624 ± 4	747 ± 2	12.3 ± 0.2	42.9
Z. Zhu [32]	60	510 ± 10	609 ± 10	34 ± 3	12.9
R. Liu [12]	123	519	601	34	/

CoCrFeMnNi HEA are mainly attributed to the planar dislocation slip of the HEA matrix [28,31]. The lack of tensile ductility and work hardening effect in this alloy will be discussed in detail later.

On the other hand, the in-situ alloyed sample performs outstandingly in compression ductility, which origins from the ductile nature of the CoCrFeMnNi HEA. A partial compression curve is provided in Fig. 2(c), as the tested sample has not failed during the test even though the strain exceeds 100%.

3.2. Microstructure and deformational behaviour

The SEM fractography of a tensile specimen is provided in Fig. 3(a). Besides typical micro-dimples similar to other CoCrFeMnNi HEAs fabricated via LPBF, plenty of microparticles can be observed inside those dimples, which is abnormal for this material [12,32]. The extensive occurrence of microparticles might be responsible for the premature failure of the material during tensile testing. In Fig. 3(b), a BSE image with inverse contrast also reveals distribution of secondary particles in the HEA substrate, as well as a cellular structure that is typical in the LPBFed HEA. The EDS line scan results indicate that the concentration of Mn and O is evidently higher in the particle compared to other alloying elements. The volumetric fraction of the particles should be small, otherwise the corresponding XRD spectrum (Fig. 4) should have shown its presence rather than the currently revealed single fcc phase. Image J analysis suggests the volume fraction of the oxide particles is around 7%.

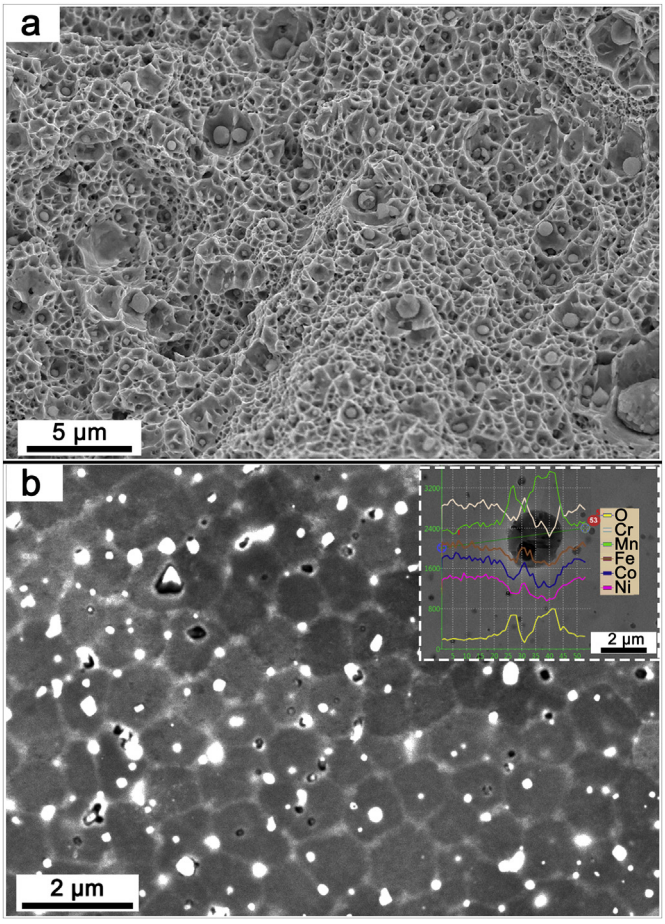

Fig. 3. (a) The SEM fracture surface of a tensile specimen. (b) BSE-ECCI image of as-built HEA revealing bright oxide particles and cellular structure, embedded with an EDS line scanning of an oxide particle.

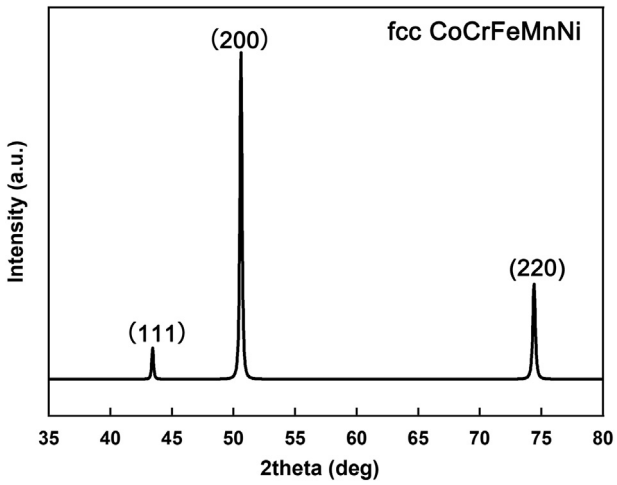

Fig. 4. The XRD spectrum of the in-situ alloyed CoCrFeMnNi HEA, showing a single-phase fcc structure.

TEM has been employed to further identify these particles. Fig. 5(a) and Fig. 3 reveal a homogeneous distribution of near-spherical particles, with an average size of ~100 nm. Irregularly-shaped particles of few micrometres in size were occasionally observed as well. Since the elemental Mn powder has a much larger Dv10 of ~7 μm, these particles were in-situ formed during the LPBF process, rather than being from the original powder. To investigate the crystal structure, selected area diffraction (SAD) analysis was conducted on the spherical particles. SAD patterns and EDS mapping results of a particle-containing area are shown in Fig. 5(b). The fcc HEA matrix contains homogeneous distributions of all alloying elements including Mn. The particles were rich in Mn and oxygen as expected. The electron diffraction information indicated the particle to be the Mn_2O_3 phase. Such phase has also been found in an LPBFed CoCrFeMnNi HEA fabricated using pre-alloyed powder [33]. Distribution of the ceramic Mn_2O_3 material in the current alloy is, however, extensive, which should have influenced the deforming behaviour and mechanical properties dramatically.

In order to investigate the influence of oxide particles on deformation, microstructures of samples in both as-built and deformed condition have been characterised. The inverse pole figure (IPF) maps of cross-sections normal to the building direction (z-axis) are shown in Fig. 6(a, e). Most of the coarse grains align along x and y-axis, which are scanning directions. Meanwhile, finer grains fill in gaps between arrays of coarse grains. This characteristic grain geometry in the xy-planes is a consequence of scanning route and can vary according to scanning strategies. In comparison, there is no obvious change in grain geometry after tensile deformation, and mechanical twins have not been found. Although the twinning effect is considered responsible to both the deformability and work hardening tendency in the CoCrFeMnNi HEA, the initiation of twins normally requires high strain rate as well as cryogenic temperature [28,30]. As for the CoCrFeMnNi HEA fabricated via LPBF, the occurrence of nano-twins has been observed in samples with tensile strain higher than 20% [12]. It is deduced that twins have not occurred in this study because the failure happens within 15% strain. By comparing kernel average misorientation (KAM) maps before and after deformation, the accumulation of misorientations occurs not only at the grain boundaries but also around oxide particles as shown in the embedded pictures (Fig. 6(b, f)), hence the in-situ alloyed HEA can be strengthened by the extra dislocations. Pole Figures (PFs) are provided in Fig. 6(c, g). The (001) orientation, which is the preferred growing direction of the fcc HEA along heat gradient, gathers at either the building direction or the scanning directions, indicating the heat gradient is affected by scanning strategy as well [34]. After tensile deformation in the y-direction, the distortion of grain is also reflected as

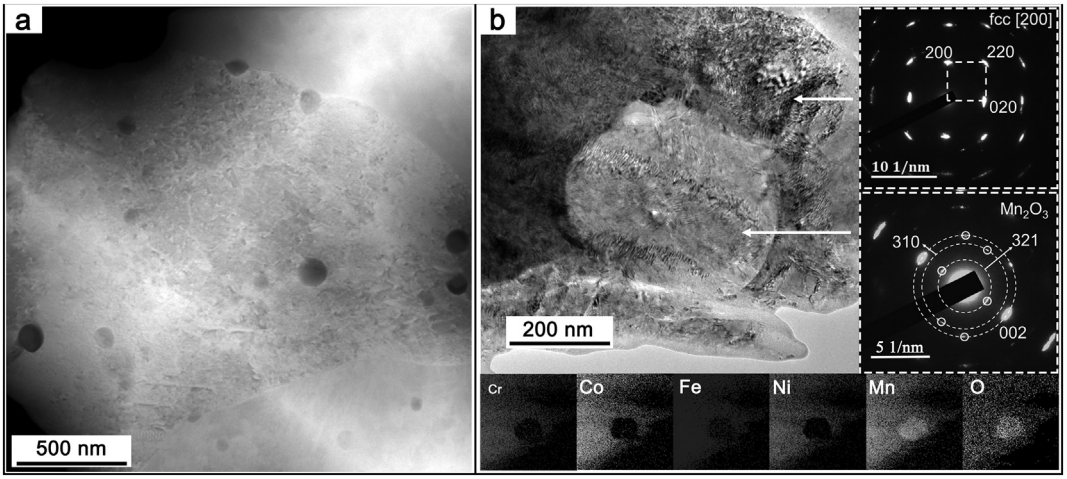

Fig. 5. (a) A scanning transmission electron microscopy (STEM) image showing the distribution of particles in the HEA, and (b) TEM EDS mapping results with embedded SAD patterns of the HEA matrix a particle.

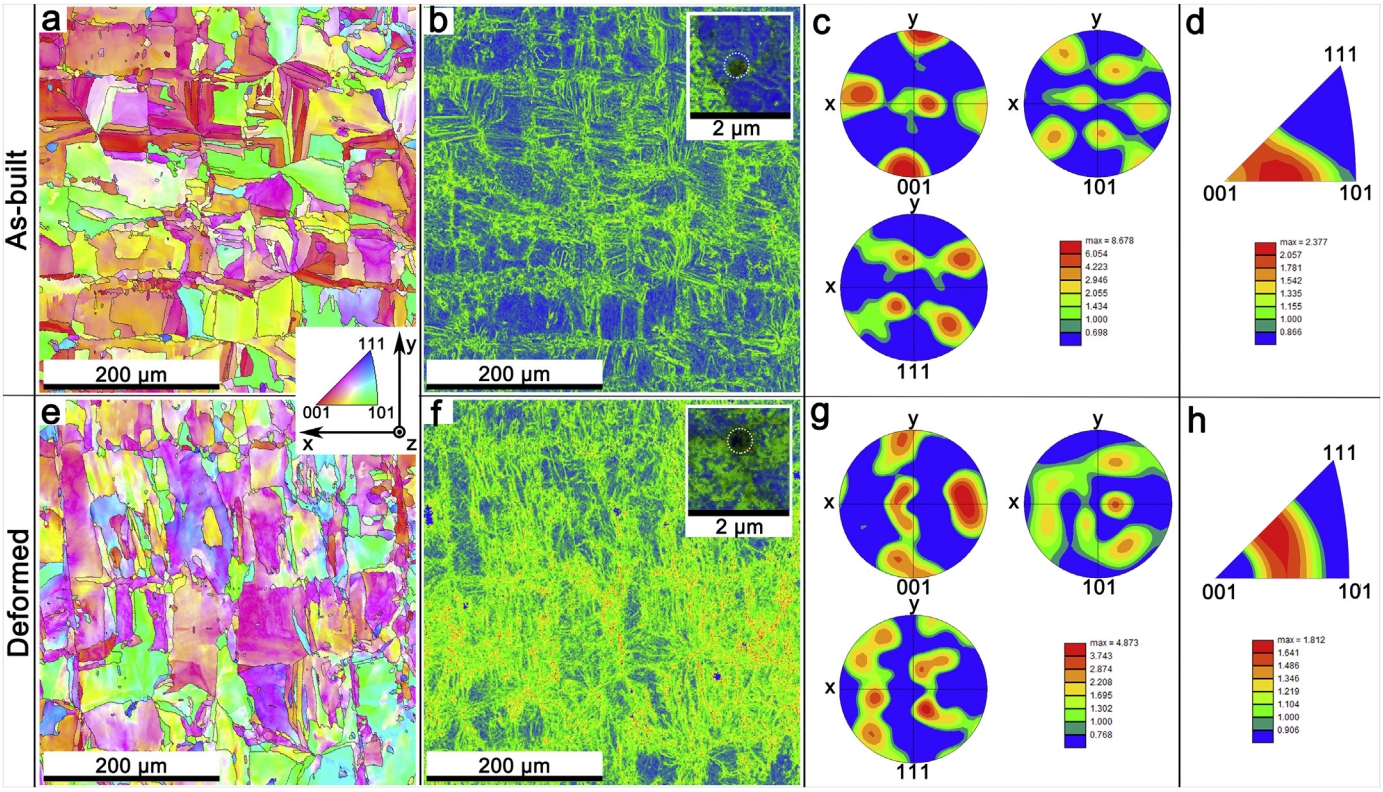

Fig. 6. (a, e) IPF maps, (b, f) KAM maps with embedded pictures showing areas around oxide particles, (c, g) PFs, and (d, h) IPFs as-built and deformed HEA samples.

stretches along the y-axis. Besides that, the (001) texture is weaker due to the distortion according to the IPFs in Fig. 6(d, h).

As the deformational behaviour of the in-situ alloyed HEA is most likely related to the oxide particles, the morphology of the oxide particles and dislocations are revealed by ECCI. In the as-built status (Fig. 7 (a)), oxide particles are mostly round and rarely surrounded by massive dislocations. After deformation (Fig. 7(b)), besides the occurrence of slip bands, dislocations have grown obviously inside grains, especially in areas around the oxide particles that generate massive clusters of dislocations. Several oxide particles are pointed out in the deformed sample by arrows. These particles locate inside slip bands and their contour profile has been stretched along the slip band, therefore transforming into spindle shapes.

TEM has been performed to investigate the transformation in these regions. Fig. 8(a) shows an oxide particle crossed by a slip band. Two gaps are observed on symmetrical positions of the particles. Meanwhile, they also locate on opposite sides of the slip band. Fig. 8(b) shows a spindle structure consisting of an oxide particle and two enlarged triangle spacings, which corresponds to those spindle areas observed in the ECCI image at the lower magnification. The SAD patterns embedded in Fig. 8(c) show that there are MnO particles in the matrix other than Mn_2O_3.

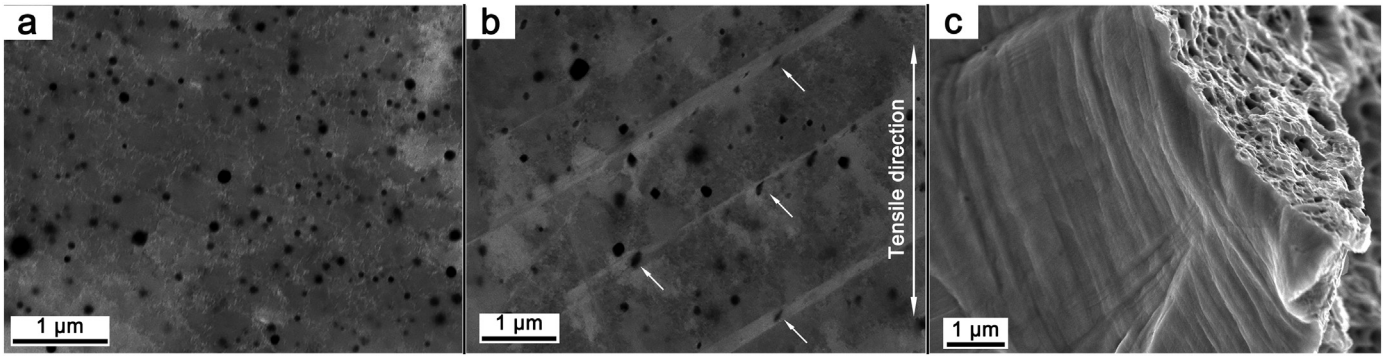

Fig. 7. The distribution of dislocations and oxide particles are revealed in ECCI images of (a) the as-built HEA, and (b) a tested tensile specimen. (c) An SEM image of the slide lines in the fracture surface.

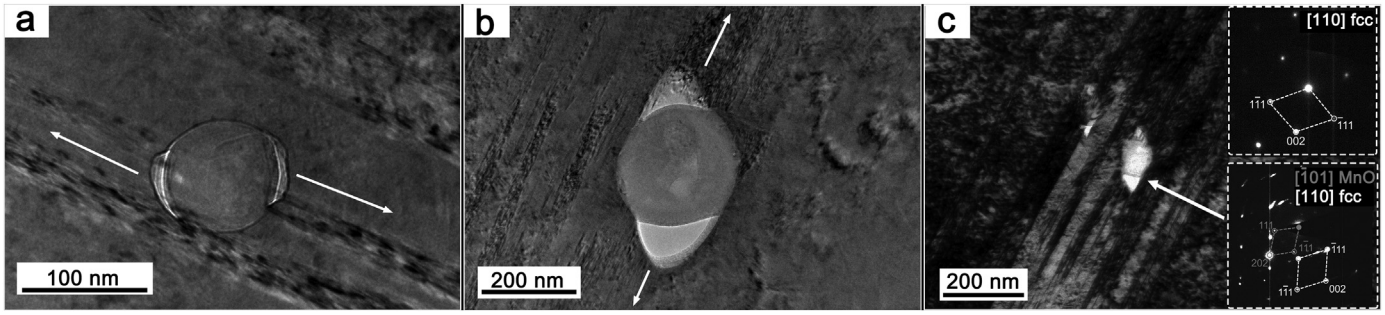

Fig. 8. (a, b) TEM bright-field images of oxide particles and micro-voids formed around them after deformation. (c) A TEM dark-field image with SAD patterns of the HEA matrix and the oxide particle.

Although TEM images were not taken in in-situ tensile tests, the deformation behaviour can still be deduced that when the HEA matrix moves towards opposite directions as arrows marked in Fig. 8 (a, b), gaps occur due to weak bonding and difference in stiffness between oxide particles and the HEA matrix [35]. As the displacement increases, they gradually grow into larger voids that leads to the failure of the material. There have been reports on LPBFed CoCrFeMnNi HEAs strengthened via introducing secondary phases particles such as TiN and carbide, but the dynamic interaction between the particles and the matrix remains absent [14,36]. The abundance of oxide particles in the in-situ alloyed HEA creates a much higher density of sub-micron voids that result in early fracture during the tensile deformation, which also explains those oxide particles present in dimples. On the other hand, dispersed oxide particles hinder the plastic deformation, reinforcing the in-situ alloyed HEA and making it a kind of oxide-dispersion-strengthened (ODS) HEA.

4. Discussion

Along with the results of a previous study [23], the above experimental results demonstrate that as long as an appropriate powder mixing procedure and optimised printing parameters are adopted, a crack-free CoCrFeMnNi HEA with compositional homogeneity can be realised by the powder-mixture and then laser in-situ alloying approach, and by using Mn as a secondary powder to add into the quaternary, pre-alloyed CoCrFeNi HEA powder. It is important to add that cracks may still form if the heat input parameters are too excessive, leading for instance to solidification cracking or cracking due to residual stresses. Still, the process parameters need to be optimised to ensure achieving chemical homogeneity during in-situ alloying with Mn-doping.

A few important phenomena involved in the approach, however, need to be clarified, which are discussed as follows.

4.1. Strengthening mechanism

For the CoCrFeMnNi HEA fabricated via LPBF, grain boundary strengthening and dislocation strengthening (σ_{dis}) are considered as the two major strengthening mechanisms. The deformation behaviours observed in this study indicate the oxide particles act as strong obstacles despite their difference in size (see Fig. 7 and Fig. 8), which is non-shearable for dislocations [14,37]. The Orowan strengthening (σ_O) is therefore also applied to understand the mechanical performance of the in-situ alloyed HEA. The overall estimated yield strength can be expressed as follows:

$$\sigma_y = \sigma_{HP} + \sigma_{dis} + \sigma_O \quad (1)$$

The term σ_{HP} summarises the grain boundary strengthening by the Hall-Petch relationship [28]:

$$\sigma_{HP} = \sigma_0 + kd^{-1/2} \quad (2)$$

where σ_0 is the friction stress, k is the Hall-Petch coefficient and d is the grain size which is 42.9 μm in this study. Based on the σ_0 of 194 MPa and k of 490 MPa μm$^{1/2}$ that is typically applied to the CoCrFeMnNi HEA [38], σ_{HP} is calculated to be ~269 MPa.

The term dislocation strengthening is expressed as follows [32]:

$$\sigma_{dis} = \alpha MGb\sqrt{\rho} \quad (3)$$

where α is a constant. M, G and b denote the Taylor factor (3.06 for fcc HEA), the shear modulus (80 GPa [39]), and the Burgers vector (0.255 nm [30]), respectively. In the CoCrFeMnNi HEA fabricated via LPBF, most of the dislocations are stored in the cellular walls of the

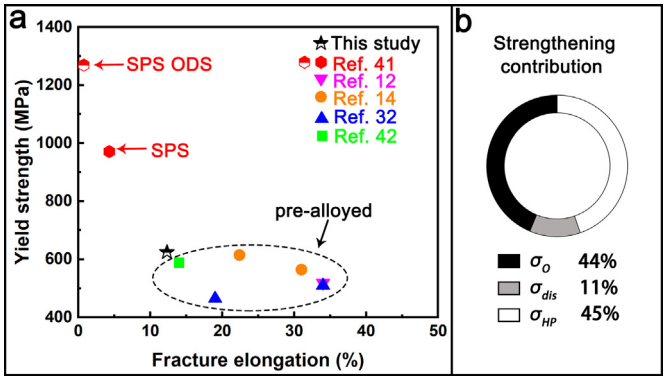

Fig. 9. (a) Comparison of tensile properties of CoCrFeMnNi HEAs fabricated via LPBF using pre-alloyed powder, and ODS CoCrFeMnNi HEA fabricated via SPS [12,14,32,41,42], and (b) an illustration of estimated contribution from each strengthening mechanism.

sub-grain structure (Fig. 3(a)). Therefore, the dislocation density (ρ) can be estimated according to the correlation below [40]:

$$\sqrt{\rho} = c/\lambda \tag{4}$$

where λ stands for the cell size which is 0.89 μm in this study. c is a constant as well as the α, and their product is closed to one [40]. In addition, the contribution of dislocation strengthening is calculated to be ~70 MPa in the in-situ alloyed HEA.

The Orowan strengthening is an untypical strengthening mechanism for the single-phase CoCrFeMnNi HEA. Although nano-precipitations has been observed in some LPBFed HEAs, their reinforcement to the strength is neglectable due to their low volume fraction. In the in-situ alloyed HEA, the Orowan strengthening is considerable because those oxide particles are widely dispersed into the HEA matrix, and its impact can be further expressed as follows [33]:

$$\sigma_O = \frac{0.4M}{\pi\sqrt{1-\nu}}\frac{Gb}{L}\ln\left(\sqrt{\frac{2}{3}}d_o/b\right) \tag{5}$$

where ν denotes the Poisson's ratio (0.26 [14]). L and d_o represent the inter-particle spacing and mean particle diameter of oxide particles. L can be calculated via the equation shown below:

$$L = \sqrt{\frac{2}{3}}d_o\sqrt{\frac{\pi}{4f}-1} \tag{6}$$

where f is the volume fraction of oxide particles.

In this study, the d_o (87 nm) and f (0.068) are measured via particle counting on cross-sections (ImageJ). By using Eq. (5) and Eq. (6), the estimated strengthening contribution from the Orowan strengthening is ~263 MPa. In addition, the theoretical yield strength calculated from Eq. (1) is ~602 MPa, which is closed to the experimental result. Because high volumetric energy density has been employed to homogenise the Mn distribution (Table. 2, [23]), microstructures (grain size and cell size) are coarsened by the extra energy input, while coarse microstructures could lead to a reduction in grain boundary strengthening and dislocation strengthening. Fig. 9(a) illustrates that the in-situ alloyed HEA still takes advantage over those fabricated using pre-alloy powder due to the considerable Orowan strengthening (~ 44% of all contributions to the strength), where the contributions from all the three mechanisms are summarised into Fig. 9(b). On the other hand, embrittlement due to the oxides is also noticeable in the study that employs SPS to fabricate ODS CoCrFeMnNi HEA. Similar mechanism has been observed in the LPBFed stainless steel that was fabricated using a blend of pre-alloyed powder and Y_2O_3 powder; the appearance of micro-voids causes a sudden drop in strain-hardening rate and limits the elongation of the material [35]. Nevertheless, Fig. 9(a) indicates that the presently developed material has a combination of high yield strength and moderate tensile elongation, compared with the same material but produced by different approaches. The current in-situ alloying approach is efficient to produce oxide particles but with rather coarse in size. It is possible to achieve a better combination of strength and ductility by tailoring the size distribution, for instance through applying a partially reductive atmosphere (H_2 + Ar gas mixture) in the LPBF process.

4.2. Formation of the Mn oxides during the LPBF process

Two types of Mn oxides, MnO and Mn_2O_3, have been observed in the in-situ alloyed HEA. They could either exist in the raw powder or form due to in-situ oxidation. Regarding the mechanism, the following discussion can be made. Firstly, Mn is a reactive element and hence the surface of the Mn powder can be oxidised after fabrication, resulting in a shell of surface oxide. The outermost surface of the Mn elemental powder used in this study is analysed via XPS to confirm this, and the spectra are provided in Fig. 6. As expected, Mn and O are both detected in the survey spectrum (Fig. 6(a)), where the peaks of C used for calibration are shown as well. To determine the Mn oxidation states, a fine scan is operated near Mn2p, which is the primary XPS region of Mn (binding energy of $Mn2p_{3/2}$, ~ 638.7 eV). Although Mn^{2+} possesses the same $Mn2p_{3/2}$ peak at 641.4 eV as Mn^{3+}, its characteristic satellite feature (~647 eV) does not appear in Fig. 6(b). The results imply that the oxide covering the original elemental Mn powder is identified as Mn_2O_3, which matches the TEM result in Fig. 5(b). The Mn_2O_3 layer

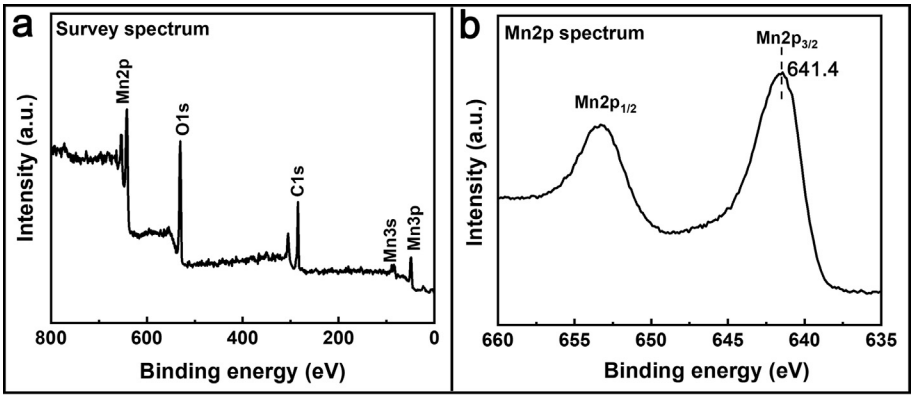

Fig. 10. The Mn2p XPS spectra measured from the surface of the Mn elemental powder, (a) survey scan and (b) fine scan on the Mn2p peaks.

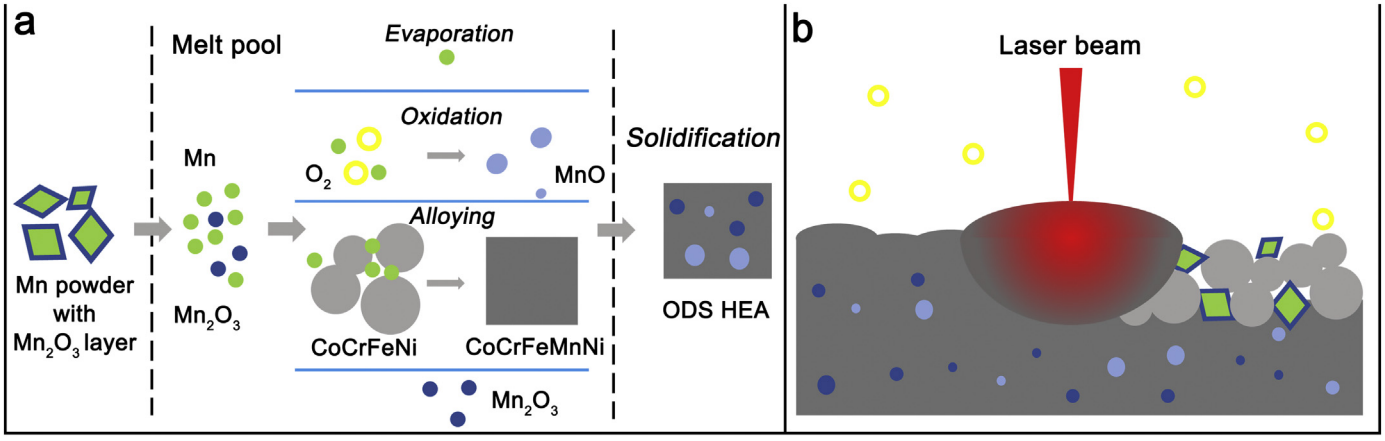

Fig. 11. (a) The in-situ reaction of the Mn elemental powder. (b) A schematic showing the transformation of materials in the LPBF process.

can be melted and subsequently mixed into the matrix during the LPBF process, remaining as Mn_2O_3 particles in the in-situ alloyed HEA [43]. It is known that Mn_2O_3 can deoxygenate to form Mn_3O_4 in either oxidising or non-oxidising atmosphere (~1050 °C), but Mn_3O_4 particle has not been observed in this study. Furthermore, its change to MnO requires a reducing atmosphere (e.g. H_2) [44], which is not the case of the present study (Fig. 10).

Besides the remnant from the elemental Mn powder, in-situ oxidation is hardly evitable during the LPBF process due to the high chemical reactivity of Mn for oxygen, which can be another source of the oxides. This can be argued as follows: Although the atmospheric oxygen level in the building chamber is normally lowered down to 0.2% before printing, there is still residual oxygen in powder as well as the atmosphere that can react with the powder [26,27]. The oxygen content increases from ~3051 ppm in the blended powder, to ~3310 ppm in the as-built sample, indicating in-situ oxidation during the LPBF process. In this study, MnO is found in the as-built HEA other than the Mn_2O_3 as mentioned above. The Gibbs energy of formation (ΔG_f^0) for MnO is lower than that for Cr_2O_3 (e.g. at 1100 K: MnO -610 kJ/mol [45] vs. Cr_2O_3–565 kJ/mol [26]), which is the most stable binary oxide among the elements from the pre-alloyed powder [46]. A study on the oxidation of $CoCrFeNiAl_{0.1}$ HEA indicated that this HEA system possesses better resistance to oxidation compared with some conventional alloys. Meanwhile, it was pointed out by the study that the oxides were primarily Cr_2O_3, alongside Al_2O_3 [47]. As Cr_2O_3 has not been observed in the present HEA, the formation of other binary oxides (e.g. NiO, Fe_2O_3) is further less possible. Moreover, although some ternary oxides such as $(Mn, Cr)_3O_4$ system can be thermodynamically favourable, their formation requires a long holding time at elevated temperatures, which is not the case in the present LPBF process [26,48]. Hence, the in-situ reaction of the elemental Mn powder is illustrated in Fig. 11(a), to explain the occurrence of MnO and Mn_2O_3 particles in the in-situ alloyed HEA. Fig. 11(b) shows the process of laser scanning over the powder bed of the blended powder.

5. Conclusions

By combining the novelty of HEA and compositional flexibility of LPBF in-situ alloying, this research reveals the possibility of developing LPBFed high-performance HEAs. Conclusions can be made as follows.

a. A blend of pre-alloyed CoCrFeN powder and elemental Mn powder has been used to in-situ fabricate CoCrFeMnNi HEA via LPBF. The process results in an ODS HEA that consists of fcc CoCrFeMnNi matrix with ~7% volumetric fraction of Mn oxide particles. A combination of high tensile strength (630/730 as the yield/fracture strengths) and moderate tensile ductility (~12%) has been achieved by the LPBFed, oxide-dispersion-strengthened CoCrFeMnNi HEA. The developed HEA also maintained high compression ductility.
b. The strength of the in-situ alloyed HEA is mainly reinforced by the Orowan strengthening compared to those CoCrFeMnNi HEAs fabricated using pre-alloyed powder. Sub-micron oxide particles hinder the plastic deformation of the matrix, generating voids along the slip directions and reducing the tensile ductility to a certain degree.
c. Oxide particles in the ODS HEA are recognised to be Mn_2O_3 and MnO. The Mn_2O_3 phase is most likely resulted from remelting of the oxide surface of elemental Mn powder, while the MnO particles should be due to the in-situ oxidation reaction between Mn and oxygen during the LPBF process.

Author credits

The paper is an output of the PhD project of PC, co-supervised by MY and MMA, as a joint PhD project between the Southern University of Science and Technology (SUSTech) and the University of Birmingham (UoB). PC fabricated the samples at UoB with assistance from SL, and performed the microstructural and mechanical properties characterisation at SUSTech, assisted by YC. All authors reviewed the manuscript.

Declaration of Competing Interest

None.

Acknowledgements

This research is supported by Shenzhen Science and Technology Innovation Commission [ZDSYS201703031748354 and JCYJ20170817110358927]; Science and Technology Planning Project of Guangdong Province of China [grant number 2017B090911003], Natural Science Foundation of Guangdong Province [2016A030313756]. Dr. M. Yan appreciates the support of Humboldt Research Fellowship for Experienced Researchers. The authors acknowledge the assistance of SUSTech Core Research Facilities. The authors also acknowledge the facilities, and the scientific and technical assistance of the RMIT University's Microscopy & Microanalysis Facility, a linked laboratory of the Microscopy Australia.

References

[1] Y. Zhang, T.T. Zuo, Z. Tang, M.C. Gao, K.A. Dahmen, P.K. Liaw, Z.P. Lu, Microstructures and properties of high-entropy alloys, Prog. Mater. Sci. 61 (2014) 1–93, https://doi.org/10.1016/j.pmatsci.2013.10.001.

[2] J.W. Yeh, Recent progress in high-entropy alloys, Ann. Chim-Sci Mat. 31 (6) (2006) 633–648, https://doi.org/10.3166/acsm.31.633-648.

[3] D.B. Miracle, O.N. Senkov, A critical review of high entropy alloys and related concepts, Acta Mater. 122 (2017) 448–511, https://doi.org/10.1016/j.actamat.2016.08.081.

[4] J.W. Yeh, S.K. Chen, S.J. Lin, J.Y. Gan, T.S. Chin, T.T. Shun, C.H. Tsau, S.Y. Chang, Nanostructured high-entropy alloys with multiple principal elements: novel alloy design concepts and outcomes, Adv. Eng. Mater. 6 (5) (2004) 299–303, https://doi.org/10.1002/adem.200300567.

[5] J.Y. He, W.H. Liu, H. Wang, Y. Wu, X.J. Liu, T.G. Nieh, Z.P. Lu, Effects of Al addition on structural evolution and tensile properties of the FeCoNiCrMn high-entropy alloy system, Acta Mater. 62 (2014) 105–113, https://doi.org/10.1016/j.actamat.2013.09.037.

[6] Z. Li, K.G. Pradeep, Y. Deng, D. Raabe, C.C. Tasan, Metastable high-entropy dual-phase alloys overcome the strength-ductility trade-off, Nature 534 (7606) (2016) 227–230, https://doi.org/10.1038/nature17981.

[7] J.Y. He, H. Wang, H.L. Huang, X.D. Xu, M.W. Chen, Y. Wu, X.J. Liu, T.G. Nieh, K. An, Z.P. Lu, A precipitation-hardened high-entropy alloy with outstanding tensile properties, Acta Mater. 102 (2016) 187–196, https://doi.org/10.1016/j.actamat.2015.08.076.

[8] S. Singh, N. Wanderka, B.S. Murty, U. Glatzel, J. Banhart, Decomposition in multi-component AlCoCrCuFeNi high-entropy alloy, Acta Mater. 59 (1) (2011) 182–190, https://doi.org/10.1016/j.actamat.2010.09.023.

[9] D. Zhang, S. Sun, D. Qiu, M.A. Gibson, M.S. Dargusch, M. Brandt, M. Qian, M. Easton, Metal alloys for fusion-based additive manufacturing, Adv. Eng. Mater. 20 (5) (2018)https://doi.org/10.1002/adem.201700952.

[10] T. DebRoy, H.L. Wei, J.S. Zuback, T. Mukherjee, J.W. Elmer, J.O. Milewski, A.M. Beese, A. Wilson-Heid, A. De, W. Zhang, Additive manufacturing of metallic components – process, structure and properties, Prog. Mater. Sci. 92 (2018) 112–224, https://doi.org/10.1016/j.pmatsci.2017.10.001.

[11] Y. Brif, M. Thomas, I. Todd, The use of high-entropy alloys in additive manufacturing, Scr. Mater. 99 (2015) 93–96, https://doi.org/10.1016/j.scriptamat.2014.11.037.

[12] R. Li, P. Niu, T. Yuan, P. Cao, C. Chen, K. Zhou, Selective laser melting of an equiatomic CoCrFeMnNi high-entropy alloy: Processability, non-equilibrium microstructure and mechanical property, J. Alloys Compd. 746 (2018) 125–134, https://doi.org/10.1016/j.jallcom.2018.02.298.

[13] P.F. Zhou, D.H. Xiao, Z. Wu, X.Q. Ou, Al0.5FeCoCrNi high entropy alloy prepared by selective laser melting with gas-atomized pre-alloy powders, Mater. Sci. Eng. A 739 (2019) 86–89, https://doi.org/10.1016/j.msea.2018.10.035.

[14] J.M. Park, J. Choe, J.G. Kim, J.W. Bae, J. Moon, S. Yang, K.T. Kim, J.-H. Yu, H.S. Kim, Superior tensile properties of 1%C-CoCrFeMnNi high-entropy alloy additively manufactured by selective laser melting, Mater. Res. Lett. (2019) 1–7, https://doi.org/10.1080/21663831.2019.1638844.

[15] T. Fujieda, M. Chen, H. Shiratori, K. Kuwabara, K. Yamanaka, Y. Koizumi, A. Chiba, S. Watanabe, Mechanical and corrosion properties of CoCrFeNiTi-based high-entropy alloy additive manufactured using selective laser melting, Addit. Manuf. 25 (2019) 412–420, https://doi.org/10.1016/j.addma.2018.10.023.

[16] S. Luo, C. Zhao, Y. Su, Q. Liu, Z. Wang, Selective laser melting of dual phase AlCrCuFeNix high entropy alloys: formability, heterogeneous microstructures and deformation mechanisms, Addit. Manuf. 31 (2020) 100925, https://doi.org/10.1016/j.addma.2019.100925.

[17] R. Zhou, Y. Liu, C. Zhou, S. Li, W. Wu, M. Song, B. Liu, X. Liang, P.K. Liaw, Microstructures and mechanical properties of C-containing FeCoCrNi high-entropy alloy fabricated by selective laser melting, Intermetallics 94 (2018) 165–171, https://doi.org/10.1016/j.intermet.2018.01.002.

[18] W. Wu, R. Zhou, B. Wei, S. Ni, Y. Liu, M. Song, Nanosized precipitates and dislocation networks reinforced C-containing CoCrFeNi high-entropy alloy fabricated by selective laser melting, Mater. Charact. 144 (2018) 605–610, https://doi.org/10.1016/j.matchar.2018.08.019.

[19] J. Joseph, T. Jarvis, X. Wu, N. Stanford, P. Hodgson, D.M. Fabijanic, Comparative study of the microstructures and mechanical properties of direct laser fabricated and arc-melted AlxCoCrFeNi high entropy alloys, Mater. Sci. Eng. A 633 (2015) 184–193, https://doi.org/10.1016/j.msea.2015.02.072.

[20] Z.H. Zhang, Y.H. Zhou, S.Y. Zhou, L. Zhang, M. Yan, Mechanically blended Al: simple but effective approach to improving mechanical property and thermal stability of selective laser-melted Inconel 718, Metall. Mater. Trans. A 50 (8) (2019) 3922–3936, https://doi.org/10.1007/s11661-019-05299-6.

[21] A. Grigoriev, I. Polozov, V. Sufiiarov, A. Popovich, In-situ synthesis of Ti2AlNb-based intermetallic alloy by selective laser melting, J. Alloys Compd. 704 (2017) 434–442, https://doi.org/10.1016/j.jallcom.2017.02.086.

[22] I. Polozov, V. Sufiiarov, A. Popovich, D. Masaylo, A. Grigoriev, Synthesis of Ti-5Al, Ti-6Al-7Nb, and Ti-22Al-25Nb alloys from elemental powders using powder-bed fusion additive manufacturing, J. Alloys Compd. 763 (2018) 436–445, https://doi.org/10.1016/j.jallcom.2018.05.325.

[23] P. Chen, S. Li, Y. Zhou, M. Yan, M.M. Attallah, Fabricating CoCrFeMnNi high entropy alloy via selective laser melting in-situ alloying, J. Mater. Sci. Technol. 43 (2020) 40–43, https://doi.org/10.1016/j.jmst.2020.01.002.

[24] H. Prasad, S. Singh, B.B. Panigrahi, Mechanical activated synthesis of alumina dispersed FeNiCoCrAlMn high entropy alloy, J. Alloys Compd. 692 (2017) 720–726, https://doi.org/10.1016/j.jallcom.2016.09.080.

[25] B. Gwalani, R.M. Pohan, O.A. Waseem, T. Alam, S.H. Hong, H.J. Ryu, R. Banerjee, Strengthening of Al0.3CoCrFeMnNi-based ODS high entropy alloys with incremental changes in the concentration of Y2O3, Scr. Mater. 162 (2019) 477–481, https://doi.org/10.1016/j.scriptamat.2018.12.021.

[26] H. Springer, C. Baron, A. Szczepaniak, E.A. Jägle, M.B. Wilms, A. Weisheit, D. Raabe, Efficient additive manufacturing production of oxide- and nitride-dispersion-strengthened materials through atmospheric reactions in liquid metal deposition, Mater. Des. 111 (2016) 60–69, https://doi.org/10.1016/j.matdes.2016.08.084.

[27] C. Qiu, A new approach to synthesise high strength nano-oxide dispersion strengthened alloys, J. Alloys Compd. 790 (2019) 1023–1033, https://doi.org/10.1016/j.jallcom.2019.03.221.

[28] Z. Li, S. Zhao, R.O. Ritchie, M.A. Meyers, Mechanical properties of high-entropy alloys with emphasis on face-centered cubic alloys, Prog. Mater. Sci. 102 (2019) 296–345, https://doi.org/10.1016/j.pmatsci.2018.12.003.

[29] S. Guan, D. Wan, K. Solberg, F. Berto, T. Welo, T.M. Yue, K.C. Chan, Additive manufacturing of fine-grained and dislocation-populated CrMnFeCoNi high entropy alloy by laser engineered net shaping, Mater. Sci. Eng. A 761 (2019)https://doi.org/10.1016/j.msea.2019.138056.

[30] G. Laplanche, A. Kostka, O.M. Horst, G. Eggeler, E.P. George, Microstructure evolution and critical stress for twinning in the CrMnFeCoNi high-entropy alloy, Acta Mater. 118 (2016) 152–163, https://doi.org/10.1016/j.actamat.2016.07.038.

[31] B. Gludovatz, E.P. George, R.O. Ritchie, Processing, microstructure and mechanical properties of the CrMnFeCoNi High-Entropy Alloy, JOM 67 (10) (2015) 2262–2270, https://doi.org/10.1007/s11837-015-1589-z.

[32] Z.G. Zhu, Q.B. Nguyen, F.L. Ng, X.H. An, X.Z. Liao, P.K. Liaw, S.M.L. Nai, J. Wei, Hierarchical microstructure and strengthening mechanisms of a CoCrFeNiMn high entropy alloy additively manufactured by selective laser melting, Scr. Mater. 154 (2018) 20–24, https://doi.org/10.1016/j.scriptamat.2018.05.015.

[33] Y.-K. Kim, J. Choe, K.-A. Lee, Selective laser melted equiatomic CoCrFeMnNi high-entropy alloy: microstructure, anisotropic mechanical response, and multiple strengthening mechanism, J. Alloys Compd. 805 (2019) 680–691, https://doi.org/10.1016/j.jallcom.2019.07.106.

[34] A. Piglione, B. Dovgyy, C. Liu, C.M. Gourlay, P.A. Hooper, M.S. Pham, Printability and microstructure of the CoCrFeMnNi high-entropy alloy fabricated by laser powder bed fusion, Mater. Lett. 224 (2018) 22–25, https://doi.org/10.1016/j.matlet.2018.04.052.

[35] Y. Zhong, L. Liu, J. Zou, X. Li, D. Cui, Z. Shen, Oxide dispersion strengthened stainless steel 316L with superior strength and ductility by selective laser melting, J. Mater. Sci. Technol. 42 (2020) 97–105, https://doi.org/10.1016/j.jmst.2019.11.004.

[36] B. Li, B. Qian, Y. Xu, Z. Liu, F. Xuan, Fine-structured CoCrFeNiMn high-entropy alloy matrix composite with 12 wt% TiN particle reinforcements via selective laser melting assisted additive manufacturing, Mater. Lett. 252 (2019) 88–91, https://doi.org/10.1016/j.matlet.2019.05.108.

[37] F. Siska, L. Stratil, H. Hadraba, S. Fintova, I. Kubena, V. Hornik, R. Husak, D. Bartkova, T. Zalezak, Strengthening mechanisms of different oxide particles in 9Cr ODS steel at high temperatures, Mater. Sci. Eng. A 732 (2018) 112–119, https://doi.org/10.1016/j.msea.2018.06.109.

[38] S.J. Sun, Y.Z. Tian, H.R. Lin, X.G. Dong, Y.H. Wang, Z.J. Zhang, Z.F. Zhang, Enhanced strength and ductility of bulk CoCrFeMnNi high entropy alloy having fully recrystallized ultrafine-grained structure, Mater. Des. 133 (2017) 122–127, https://doi.org/10.1016/j.matdes.2017.07.054.

[39] Q. Lin, X. An, H. Liu, Q. Tang, P. Dai, X. Liao, In-situ high-resolution transmission electron microscopy investigation of grain boundary dislocation activities in a nanocrystalline CrMnFeCoNi high-entropy alloy, J. Alloys Compd. 709 (2017) 802–807, https://doi.org/10.1016/j.jallcom.2017.03.194.

[40] U.F. Kocks, H. Mecking, Physics and phenomenology of strain hardening: the FCC case, Prog. Mater. Sci. 48 (3) (2003) 171–273, https://doi.org/10.1016/S0079-6425(02)00003-8.

[41] H. Hadraba, Z. Chlup, A. Dlouhy, F. Dobes, P. Roupcova, M. Vilemova, J. Matejicek, Oxide dispersion strengthened CoCrFeNiMn high-entropy alloy, Mater. Sci. Eng. A 689 (2017) 252–256, https://doi.org/10.1016/j.msea.2017.02.068.

[42] Y.H. Zhou, Z.H. Zhang, Y.P. Wang, G. Liu, S.Y. Zhou, Y.L. Li, J. Shen, M. Yan, Selective laser melting of typical metallic materials: An effective process prediction model developed by energy absorption and consumption analysis, Addit. Manuf. 25 (2019) 204–217, https://doi.org/10.1016/j.addma.2018.10.046.

[43] C. Tan, K. Zhou, W. Ma, L. Min, Interfacial characteristic and mechanical performance of maraging steel-copper functional bimetal produced by selective laser melting based hybrid manufacture, Mater. Des. 155 (2018) 77–85, https://doi.org/10.1016/j.matdes.2018.05.064.

[44] M.I. Zaki, M.A. Hasan, L. Pasupulety, K. Kumari, Thermochemistry of manganese oxides in reactive gas atmospheres: probing redox compositions in the decomposition course MnO2 → MnO, Thermochim. Acta 303 (2) (1997) 171–181, https://doi.org/10.1016/S0040-6031(97)00258-X.

[45] K.T. Jacob, A. Kumar, Y. Waseda, Gibbs energy of formation of MnO: measurement and assessment, J. Phase Equilib. Diffus. 29 (3) (2008) 222–230, https://doi.org/10.1007/s11669-008-9280-5.

[46] M. Hasegawa, Ellingham Diagram, in: S. Seetharaman (Ed.), Treatise on Process Metallurgy, Elsevier 2014, pp. 507–516.

[47] H.S. Grewal, R.M. Sanjiv, H.S. Arora, R. Kumar, A. Ayyagari, S. Mukherjee, H. Singh, Activation energy and high temperature oxidation behavior of multi-principal element alloy, Adv. Eng. Mater. 19 (11) (2017)https://doi.org/10.1002/adem.201700182.

[48] F. Ye, Z. Jiao, Y. Yang, Effect of medium temperature precipitation phase and Mn element diffusion mechanism on high temperature oxidation process of repair and remanufacture CoCrFeMnNi high-entropy alloy cladding, Mater. Res. Exp. 6 (5) (2019) https://doi.org/10.1088/2053-1591/ab01be.